LLNL-JRNL-411897

LAWRENCE
LIVERMORE
NATIONAL
LABORATORY

Driving toroidally asymmetric current through the tokamak scrape-off layer, Part I: Potential for ELM suppression

I. Joseph, R. H. Cohen, D. D. Ryutov

April 6, 2009

Physics of Plasmas

Disclaimer

This document was prepared as an account of work sponsored by an agency of the United States government. Neither the United States government nor Lawrence Livermore National Security, LLC, nor any of their employees makes any warranty, expressed or implied, or assumes any legal liability or responsibility for the accuracy, completeness, or usefulness of any information, apparatus, product, or process disclosed, or represents that its use would not infringe privately owned rights. Reference herein to any specific commercial product, process, or service by trade name, trademark, manufacturer, or otherwise does not necessarily constitute or imply its endorsement, recommendation, or favoring by the United States government or Lawrence Livermore National Security, LLC. The views and opinions of authors expressed herein do not necessarily state or reflect those of the United States government or Lawrence Livermore National Security, LLC, and shall not be used for advertising or product endorsement purposes.

Driving toroidally asymmetric current through the tokamak scrape-off layer,
Part I: Potential for ELM suppression

Ilon Joseph,* Ronald H. Cohen, and Dmitri D. Ryutov

Lawrence Livermore National Laboratory

(Dated: March 30, 2009)

Abstract

A potential technique for suppressing edge localized magnetohydrodynamic instabilities (ELMs) is theoretically analyzed. Recent experiments have shown that externally generated resonant magnetic perturbations (RMPs) can stabilize ELMs by modifying the density profile [T. E. Evans, *et al.*, Nature Phys. **2**, 419 (2006); Y. Liang, *et al.*, Phys. Rev. Lett. **98**, 265004 (2007)]. Driving toroidally asymmetric current internally, through the scrape-off layer (SOL) plasma itself, can also generate RMPs that are close to the required threshold for ELM control. The limiting ion saturation current densities can be achieved by producing potential differences on the order of the electron temperature. Although the threshold is uncertain in future devices, if driven coherently though the SOL, the upper limit for the resulting field would exceed the present experimental threshold. This analysis provides the tools required for estimating the magnitude of the coherent SOL current and RMP generated via toroidally asymmetric biasing of the target. Flux expansion increases the RMP near the X-point, while phase interference due to the shearing of field lines near the X-point reduces the amplitude of the effective SOL perturbation and makes the result sensitive to both toroidal mode number n and the radial coherence width of the biasing region. If the limiting current density decays rapidly enough radially, both the width and the amplitude of the current density drawn from the target will be reduced. The RMP can still exceed the present threshold at low n if the radial location and width of the biasing region are optimally chosen.

PACS numbers: 28.52.-s,28.52.Av,52.55.Fa,52.55.Rk

Keywords: Fusion reactors, tokamaks, spherical tokamaks, power exhaust, divertors

---

*`joseph5@llnl.gov`

I. INTRODUCTION

Tokamak fusion reactors face the significant challenge of limiting the expelled charged-particle heat flux to acceptable levels for bounding wall components [1, 2], especially for the target plates that handle the regions of highest flux. This limit, fundamentally set by the atomic processes of surface melting and sublimation, is on the order of 0.5-1 $\mathrm{kW/cm^2}$ for the choices of materials currently under consideration [3]. In a reactor, large plasma instabilities that impulsively deliver energy flux to the target on fast time scales must be avoided. Aside from unanticipated disruptions, the major impulsive fluxes in an H-mode tokamak plasma are delivered by the so-called edge localized modes (ELMs). For the planned ITER facility [4], the problem is significant [5–7], but it is even more severe in follow-on high power tokamaks even when the operating point is well below ignition.

The largest ELMs, designated Type-I, are well-described by peeling-ballooning magnetohydrodynamic stability theory [8, 9] and are destabilized by both current and pressure gradients. These two instability drives are closely related at the edge of an H-mode plasma due to fact that much of the edge parallel current is driven by the bootstrap effect. Thus, for a fixed plasma geometry, reduction of the edge pressure gradient is required to operate below the ELM instability threshold. The application of resonant magnetic perturbations (RMPs) to the plasma edge breaks the toroidal symmetry of the tokamak and induces enhanced three-dimensional transport, akin to transport processes active in stellarators. This technique has been experimentally demonstrated on both DIII-D [10] and JET [11] to significantly enhance H-mode particle exhaust [12–14], allowing the plasma density and, in turn, the large edge pressure gradient to be reduced to a level below the peeling-ballooning stability threshold [12, 13]. For given plasma conditions, the success of the technique requires a threshold level of applied perturbation field $\tilde{B}$ relative to the main toroidal field B_t. Although there are still paradoxes left to be resolved as to the exact nature of the dominant transport mechanism [12, 15–17], and thus, the scaling of the threshold perturbation strength with plasma conditions, experimentally, the essential requirement is that $\tilde{B}_{mn} > 10^{-4} B_t$ for the the flux surface averaged Fourier component of the perturbation field that resonates with the pitch of the field lines at the plasma edge; i.e., $m = qn$ where q is the safety factor and m/n are the poloidal/toroidal mode numbers. Recent design studies for ITER [18, 19] have assumed threshold values $\tilde{B}_{mn}/B_t \sim 2 - 5 \times 10^{-4}$.

The possibility of controlling the edge pressure gradient and Type-I ELM stability is of major importance for future burning fusion reactors. The creation of a resonant magnetic perturbation of sufficient magnitude requires that the current-carrying coils that produce this field be placed as close as possible to the last closed plasma surface. Placing coils inside the vacuum vessel is difficult due to the engineering constraints on the maximum forces that the coils can sustain; for instance, those generated during a disruption or vertical displacement event [20]. Furthermore, it is difficult to place the coils inside of the neutron shield, because the high neutron flux will cause the insulators in the coil structure to have unreasonably short lifetimes [22].

The closest one can possibly place the perturbation currents to the plasma is on the open flux surfaces just outside the plasma interior. For a tokamak, the region of interest is the scrape-off-layer (SOL) just outside of the magnetic separatrix, where exhaust is carried along open field lines to the divertor target. When the electrostatic potential difference between the target and the plasma above the sheath is different from the floating potential, a current will be driven along the open field lines connecting to the target. The current is as close to the plasma as possible and is naturally well-aligned with the magnetic field lines near theseparatrix. Hence, the magnetic perturbation field generated in the SOL is highly resonant with field lines inside the separatrix. The main goal of the present analysis is to determine whether the experimentally demonstrated RMP threshold for achieving ELM control by external coils can be achieved by the SOL current technique.

Toroidally asymmetric electrostatic biasing was originally proposed [23–25] for a rather different purpose: to increase the width of the high heat flux region in the SOL by driving electrostatic convection cells that act to radially spread turbulence perpendicular to flux surfaces. Biasing was experimentally implemented on the MAST spherical tokamak [26] where a significant radial spreading of heat flux due to electrostatic convection was observed [27–29]. Thermo-electric effects produced by imbalances in radiation and plasma pressure [30, 31] can also be utilized for current drive. Ref. [23] proposed a variety of techniques that are potentially useful in a high-power tokamak environment, such as toroidally asymmetric gas puffing, wavy divertor plates, and spatially varying-conductivity divertor plates. Since these effects do not change the magnitude of the ion saturation current itself, we describe the conceptually simpler electrostatic technique throughout.

The resonant spectrum of the *applied field* is assumed to drive the effects of the perturbation on the plasma within. It is crucial to our analysis to observe that the critical thresholds for ELM control are given in terms of the applied perturbation fields. This is because, in the ELM control experiments to date, it has only been possible to measure the externally applied perturbation fields, $\tilde{\mathbf{B}}_{ext}$, and not the fields internally generated by currents within the plasma in response to the applied perturbations, $\tilde{\mathbf{B}}_{int}$. The response to resonant perturbations is particularly complicated by the fact that plasma rotation and drift flows will tend to shield the total resonant field arising from the sum $\tilde{\mathbf{B}} = \tilde{\mathbf{B}}_{ext} + \tilde{\mathbf{B}}_{int}$ in resistive MHD and drift-MHD models [32, 33]. At the same time, the linear magnetic response of a shaped toroidal plasma amplifies the least stable MHD modes and generates a different effective resonant spectrum than the applied spectrum [34, 35]. While the plasma generally reacts to the applied fields in a complex fashion, it has been experimentally demonstrated that the ELM control effects can be parameterized in terms of the magnitude of the applied field. Modeling of internal plasma processes is beyond the scope of this work.

This article is the first part of a series of two articles elaborating the analysis of this potential ELM control technique. Part I derives the magnitude of the coherent SOL current that can be produced in the scrape-off layer via toroidally asymmetric biasing of the target. The magnitude of the RMP that can be generated is estimated from the ion saturation current density that can be drawn from the divertor target. Part II (Ref. [36]) presents the details of the derivation of the spatial structure of the magnetic perturbation near the X-point and the analysis of the resonant spectrum near the separatrix.

Section II of this article describes the qualitative analysis that can be used to estimate the RMP amplitude neglecting interference effects. This perturbation strength is an estimate for the magnetic field that can be generated near the target plate and represents an order of magnitude estimate for the upper limit of the surface-averaged RMP that can be generated near the separatrix. After presenting the basic approach (Secs. II A-II B), the current density and RMP amplitude are estimated from published data for DIII-D and MAST (Sec. II D) and models for the ITER divertor (Sec. II E). For these cases, if the current density that can be drawn from the target plates were to be driven coherently through the SOL, the resulting perturbation would be large enough to exceed the current experimental ELM control threshold. Consideration of the field line behavior near the X-point in Sec. III determines the spatial structure of the current density profile in Sec. IV. Flux expansion plays an important role in increasing the magnitude of the RMP near the X-point (Sec.

V A). However, Sec. IV C shows that destructive phase interference will occur between neighboring flux surfaces above the X-point if the radial profile of the current density is wider than the *coherence width* (Eq. 23). This width depends both on the distance from the strike point and the divertor geometry. In a certain sense, short divertor legs have “twice” the coherence of long divertor legs (defined in Sec. IV B).

Section V calculates the effect of phase mixing by considering the efficiency of the SOL current drive for different current density profiles. In general, the RMP amplitude is optimized when the width of the biasing region is equal to the coherence width and is optimized at low toroidal mode number n. For a step-wise constant radial profile (Sec. V C), the effective SOL surface current is proportional to $1/n$. For an exponentially decaying profile (Sec. V D), strong phase mixing will exponentially reduce the efficiency unless the biasing region has at least one sharp radial boundary. If the edge location is optimally chosen, biasing only the inner or outer portion of the wetted area can still produce more than half of the maximum value attained for the optimal width. Using the current drive efficiency, Sec. VI estimates the magnitude of the RMP that can be driven including the effects of phase interference and reduced target current density. The largest RMPs can be produced at low n in a compact divertor with short divertor legs. The ability of the technique to control ELMs will depend on the amount of coherent SOL current that can be produced and the actual RMP threshold in future devices.

Gaussian CGS units are used throughout except when practical considerations make mixed, “engineering units” more appropriate.

II. QUALITATIVE ANALYSIS

A. Generating the Perturbations

Consider a divertor target that can actively generate a toroidally asymmetric electrostatic potential. The spatial pattern of the bias voltage over the divertor floor significantly affects the spatial pattern of the driven current. In the most flexible design, the divertor floor can be made of a number of tiles electrically insulated from each other so that each can be connected to an independent power supply. Such a system would control both the radial and the toroidal distribution of the current. In particular, one could consider biasing a radially-narrow ring on the divertor floor, with a sinusoidal toroidal variation. In a less flexible design, one can think of a divertor floor made of several independently biased toroidal segments. This latter arrangement does not allow for control of the radial structure of the current, which will be determined solely by the radial variation of plasma parameters.

It will be assumed that the SOL current density flows through a region that is radially much thinner than the minor radius. This is certainly true if the characteristic width of the current channel is set by the width of the SOL. Extremely wide distributions would not satisfy the assumption of being close to the plasma, nor would they efficiently utilize the space within the vacuum vessel. This implies that one can assume that the current flows within a relatively thin sheet near the separatrix, both along the divertor leg and over the surface of the confined plasma. Figure 1 illustrates the surface current pattern that would result from a set of 6 radially narrow biasing regions that alternate in polarity to produce a periodic perturbation with toroidal mode number $n = 3$.

The assumption of a surface current density near the separatrix leads to a simple estimate for the magnetic field perturbation strength. For observation points that are closer to the SOL current than either the poloidal or toroidal wavelength of the current density pattern, the magnetic field will appear to be produced by a surface current which is nearly constant in space. For these points, one can estimate the magnetic field perturbation by the usual formula for the tangential discontinuity in the field $[B]$ produced by a surface current density K. The estimate for the perturbation field is $\tilde{B} = [B]/2 = 2\pi K/c$, where c is the speed of light. Hence, an estimate of the surface current density allows one to estimate the magnetic field perturbation.

B. Target Plate Current Density

The maximum current density that can be made to flow through the sheath is the ion saturation current density. The simplest estimate for the current-voltage characteristic of the plasma sheath assumes that the plasma is collisional enough to keep the electron distribution function Maxwellian. Where the field lines travel from the plasma to the target, the parallel current density is given by the expression [37]:

$$J_{\parallel} = en_e \left\{ u_i - \frac{v_{te}}{2\sqrt{\pi}} \exp\left(-\frac{e\phi_s}{T_e} \right) \right\}, \tag{1}$$

where the sheath potential $\phi_s = \phi_p - \phi_w$ is the difference between the electric potential in the plasma just above the sheath ϕ_p, and the electric potential at the material wall ϕ_w. The other quantities are taken on the plasma side of the sheath: n_e is the electron density, $T_{e,i}$ are the electron and ion temperatures, $v_{te} = \sqrt{2T_e/m_e}$ is the characteristic electron thermal speed, e is the magnitude of the electron charge, and $m_{e,i}$ are the electron and ion masses. The parallel ion flow, u_i, is of the order of the sound speed $c_s = \sqrt{(\gamma_e T_e + \gamma_i T_i)/m_i}$, where T_i is the ion temperature and the adiabiatic index for each species is $\gamma_{e,i}$. For an unbiased plate, with an isothermal sheath ($\gamma_{e,i} = 1$) and equal ion and electron temperatures, the estimate for the floating potential is

$$e\phi_f = T_e \log\left(v_{te}/2\sqrt{\pi}u_i\right) \tag{2a}$$

$$\simeq \frac{1}{2}T_e \log\left(m_i/4\pi m_e\right). \tag{2b}$$

Assuming a deuterium plasma with Maxwellian electrons yields $e\phi_f/T_e = 2.8$, and more accurate estimates for the ratio $e\phi_f/T_e$ are in the range $2-4$, depending on plasma conditions.

The single probe characteristic,

$$J_{\|} = J_{sat}\left\{1 - \exp\left(e(\phi_f - \phi_s)/T_e\right)\right\}, \tag{3}$$

demonstrates that if the sheath potential is altered from ϕ_f by T_e/e, a current density on the order of the ion saturation current density,

$$J_{sat} = e n_e u_i, \tag{4}$$

will flow parallel to field lines. Assuming that the ion velocity is $u_i \sim \sqrt{(T_e + T_i)/m_i}$, one obtains the following equation relating the saturation current to the parameters of a deuterium plasma:

$$J_{sat} = 1.57\frac{\mathrm{A}}{\mathrm{cm}^2} \times \left(\frac{n}{10^{13}\mathrm{cm}^{-3}}\right)\left(\frac{T}{\mathrm{eV}}\right)^{1/2}. \tag{5}$$

When a current flows across the sheath, charge conservation requires the current to eventually return by flowing through another material surface. The actual current density that flows thus depends on the geometry of the flow pattern as well as the plasma sources that determine the electron density, temperature, and floating potential at each end of the field line. The resulting flow can be affected by the effective collection area of each material surface [24], as well as the effective circuit determined by the multiple conductors involved [25]. In the simple situation where the current flows between two surfaces with the same area and floating potential, but are biased with respect to one another with potential ϕ_b, the double probe characteristic

$$J_{\|} = J_{sat} \tanh \left(e\phi_b/2T_e\right), \tag{6}$$

shows that the ion saturation current is the maximum current that will flow.

An estimate for the surface current density also requires an estimate for the width over which the current is driven at the target. The width at the target is determined both by the radial variation of the bias potential and by the profiles of density and temperature across the target that determine J_{sat}. Figure 2 illustrates the radial profile of J_{sat} (thick black) and schematic profiles for the driven current that may possibly develop from a given biasing stategy: a step-wise constant profile (thin shaded blue), an exponentially decaying profile with a sharp outer edge resulting from biasing the inner side of the target plate (dotted red), an exponentially decaying profile with a sharp inner edge arising from biasing the outer part of the target plate (dashed green). In the figure, radial distances are defined in flux space ψ. The distance of the center of the current channel from the strike point is defined by $\delta\psi$ or by the distance δr orthogonal to flux surfaces. For a step-wise constant profile, one would use the average density J_{avg} over the full width $\Delta\psi$ or Δr orthogonal to flux surfaces. However, if the profiles are highly peaked and decay exponentially, it is conventional to use the maximum density J_{max} and the e-folding flux Λ^2 or the e-folding distance λ orthogonal to flux surfaces. For a thin current channel, the values are defined so that $K_{sat} = J_{avg}\Delta r = J_{max}\lambda$.

C. Estimating the RMP Amplitude

The estimate for the characteristic magnetic field that can be produced near the target is given by

$$\tilde{B}_{sat} = 2\pi K_{sat}/c. \tag{7}$$

In Part II, it will be shown that the SOL current-generated field is predominantly pitch-resonant near the plasma edge. If the SOL current drive were perfectly efficient, $\tilde{B}_{sat}$ would be also be an order of magnitude estimate for the RMP averaged over a flux surface near the separatrix. Section V is devoted to analyzing the reduction of SOL current drive efficiency by phase interference and more accurate estimates are described in Sec. VI. Hence, $\tilde{B}_{sat}$ is best thought of as an upper limit for the characteristic magnitude of the RMP that can be produced.

The preceding estimate requires further qualification because the resonant and non-resonant perturbation fields both vary strongly in space. The effective surface current density actually increases with flux expansion near the X-point (Sec. V A). This implies that for a configuration with "long" divertor legs, the field near the X-point is much larger than the field near the target plate, but then decays farther away. In Part II, it will be shown that $\tilde{B}_{sat}$ represents a good estimate for the average field amplitude for a certain range of flux surfaces near the edge. For a system with "short" divertor legs, $\tilde{B}_{sat}$ is already the maximum field and the RMP estimate must be reduced from $\tilde{B}_{sat}$ by the appropriate average over the surface. The precise definition of "long" vs. "short" is given in Sec. IV B.

For estimates for the fusion devices described next, we consider scenarios where the current is driven much closer to the strike point than the length of the divertor leg. In this case the divertor legs can be considered to be "long" and one can take $\tilde{B}_{sat}$ to represent an estimate for the upper limit of the RMP amplitude.

D. Estimates for DIII-D & MAST

If the biasing technique does not substantially change the plasma conditions above the target, an upper limit is given by the total parallel particle flux across the plasma wetted area of the unbiased target. Estimates for the width for current tokamaks can then be taken from Langmuir probe measurements of the parallel particle flux or other diagnostics of density and temperature. A very wide variation of divertor plasma parameters occurs in practice as power input and target density and temperature are varied. In Table I, a range of values for DIII-D and MAST is reported based on the published data described below.

For DIII-D, Refs. [38–40] report peak values for the outer strike point in the ranges $J_{sat} \sim 5 - 30$ A/cm^2 over roughly $\lambda \sim 2 - 3$ cm and show temperatures in the range $T_e \sim 20 - 40$ eV. This corresponds to densities in the range $n_e \sim 1 - 3 \times 10^{13}$ cm^{-3}. The radiative divertors observed in Ref. [41] achieve much higher densities $n_e \sim 0.5 - 2 \times 10^{14}$

cm^{-3}, at lower temperatures $T_e \sim 1-2$ eV, over similar widths, leading to even higher peak values $J_{max} \sim 10-40$ A/cm^2. Over the full range, one estimates values of $K_{sat} \sim 10-100$ A/cm and the upper limit $\tilde{B}_{sat} \sim 6-80$ G.

For MAST, Refs. [27–29] report peak values in the range $J_{max} \sim 0.5-2$ A/cm^2 corresponding to densities $n_e \sim 0.5-3 \times 10^{12}$ cm^{-3} and temperatures $T_e \sim 10-40$ eV. For MAST there can be a wide variation in divertor leg length and flux expansion at the target; here, we estimate $\lambda \sim 2-5$ cm. Over the full range, one estimates $K_{sat} \sim 0.9-10\ A/cm$ and the upper limit $\tilde{B}_{sat} \sim 0.4-6$ G.

E. Estimates for ITER

A first-principles technique to extrapolate the divertor target profiles to future fusion devices is still lacking. The decay lengths are determined by the balance between sources and transport in the SOL and depend upon the details of many different processes that may be active including MHD, turbulence, and neoclassical transport. Scaling results [6, 42, 43] have had mixed success and are not commonly agreed upon. Here, an estimate for K_{sat} will be based on the same 2D edge fluid code models that were used to evaluate the ITER divertor design. Transport is modeled by radial transport coefficients adjusted to fit midplane profiles to experimental data and cannot be considered predictive. Thus, the estimates here must be treated with caution.

The standard ITER divertor is partially detached in order to reduce heat flux at the strike point, leading to a wide range of values for plasma parameters along the target plate. Kukushkin [44] reports upon a detailed campaign of 2D edge fluid modeling for the ITER divertor using the B2-EIRENE code [45]. Figures 2 and 6 of Ref. [44], show that along the outer midplane near the separatrix $n_m \sim 4 \times 10^{13}$ cm^{-3} and $T_m \sim 200$ eV and decay to small values over 2 − 3 cm. Along the target plate $T_t \sim 1-2$ eV over the first $10-20$ cm where neutrals are strongly recycling and then rises to $T_t \sim 10-20$ eV further away. The standard 2-point model [37] for the downstream density at the target leads one to estimate $n_t = n_m T_m / 2T_t$. Right near the strike point, this leads to large peak values $n_t \sim 1-2 \times 10^{15}$ cm^{-3}, and $J_{max} \sim 200-400$ A/cm. Using the higher temperatures further along the plate, one would obtain $n_t \sim 2-4 \times 10^{14}$ cm^{-3} and $J_{max} \sim 100-300$ A/cm. Due to strong particle recycling, the width at the target and the total surface current is difficult to estimate from this data.

Modeling for the ITER base case [47] using the UEDGE code [46] is in good agreement with the B2-EIRENE model at the outer midplane. The parallel ion flux density reaches a peak of 300 A/cm^2 with a decay length of $\sim 2-3$ cm, and leads to a total parallel particle flux $K_{sat} = 830$ A/cm. This yields the upper limit $\tilde{B}_{sat} \sim 520$ G, a factor of 10^{-2} of the main toroidal field of 5.3T. This factor is $20-100$ times larger than the critical resonant field that is needed to suppress ELMS. In Table I, estimates for K_{sat} are derived by combining the previous range for J_{sat} with the UEDGE value for λ. This leads to the range $K_{sat} = 200 - 1000$ A/cm and $\tilde{B}_{sat} = 100 - 800\ G$.

III. X-POINT GEOMETRY

The X-point region plays a key role in all that follows. Therefore, here, we define the essential features of divertor geometry needed to describe the structure of the driven current density and perturbation fields near the X-point. Consider a large-aspect ratio tokamak of major radius R, minor radius a, divertor leg length ℓ, toroidal field B_t, poloidal field B_p, and plasma current I_p. Due to the axial symmetry of a tokamak along the toroidal angle ζ, the field lines are constrained to lie along the magnetic flux surfaces defined by the contours of the poloidal magnetic flux function $A_\zeta = \mathbf{A} \cdot (\partial \mathbf{x}/\partial\zeta)$; i.e., the covariant toroidal component of the vector potential in a suitable gauge. Assuming that little toroidal current flows in the vicinity of the X-point, the poloidal flux satisfies the source-free Grad-Shafranov equation which simply reduces to the Laplace equation to lowest order in distance from the X-point. For the generic X-point shown in Fig. 3(a), a system of orthogonal coordinates x, y can be always chosen to align with the separatrix so that x lies along the outer divertor leg and that y lies along the branch that connects to the inner midplane. With this choice, the coordinates $\{x, y, \zeta\}$ are only right-handed with an appropriate choice for the direction of ζ.

Since the poloidal field vanishes to first order, the vector potential can be chosen to vanish to second order,

$$A_\zeta = -RB_p' xy \tag{8}$$

where B_p' is the poloidal field gradient at the X-point. For a more general coordinate system, the magnitude is defined by the determinant of the 2-dimensional matrix of second order derivatives of A_ζ at the X-point:

$$(RB_p')^2 = |\det(\nabla_i \nabla_j A_\zeta)| \tag{9}$$

(in the constant ζ plane). In the vicinity of the X-point, the field line "equations of motion" are

$$dx/d\zeta = -xR/R_s \qquad\qquad dy/d\zeta = yR/R_s, \tag{10}$$

where the shear radius is defined by the relation $R_s \equiv B_t/B_p'$. The physical meaning of R_s can be elucidated by introducing the poloidal field scale length $r_p \equiv B_{p0}/B_p'$, defined by a normalizing poloidal field B_{p0} such as the field at the outer midplane.

The toroidal distance that a field line will travel over a poloidal field scale length is $2\pi R_s$ where $R_s \sim r_p B_t/B_{p0}$. The dimensionless ratio that regulates the ratio of toroidal to poloidal motion is

$$q_* = R_s/R = B_t/RB_p'. \tag{11}$$

This number acts like an effective "safety factor" for field lines near the X-point. The solutions to the equations of motion are

$$x = x_0 \exp(-(\zeta - \zeta_0)/q_*) \qquad\qquad y = y_0 \exp((\zeta - \zeta_0)/q_*), \tag{12}$$

given the initial conditions $x(\zeta_0) = x_0$ and $y(\zeta_0) = y_0$. The two constants of the field line motion can be taken to be

$$\psi = xy \qquad\qquad \zeta_0 = \zeta - q_* \log\sqrt{|y/x|}. \tag{13}$$

The first constant is simply the poloidal flux near the X-point, while the second constant is the field line label. The trajectories exponentially contract along the x direction aligned with the divertor leg and exponentially expand along the y direction aligned with the separatrix as the field line is traversed in the $+\zeta$ direction. The directions of contraction and expansion switch as the field line is traversed in the $-\zeta$ direction. Since the equations of motion are linear, small deviations of the trajectories also follow the same equations near the X-point. An initially circular flux tube near the divertor target will exponentially stretch along the separatrix and exponentially shrink across the separatrix as it passes in the vicinity of the X-point in the $+\zeta$ direction and vice-versa in the $-\zeta$ direction [48].

For a definite example, consider the simple two-wire model of a diverted plasma: an external coil carrying a current I_d parallel to the plasma current I_p generates a field null along the line connecting the two coils as shown in Fig. 3(b). If a is the distance from the X-point to the center of the tokamak and d is the distance from the X-point to the external coil, then the condition that the poloidal field vanishes is $I_p/a = I_d/d$. Note that a is naturally elongated relative to the minor radius at the outer midplane. Relative to the poloidal field without the divertor coil, the poloidal field gradient scale length is

$$r_p = \frac{B_{p0}}{B_p'} \simeq \frac{1}{(a^{-1} + d^{-1})}. \tag{14}$$

In the case of a compact divertor where $d << a$, $r_p = d$, while for equal plasma and coil currents ($I_p = I_d$), $r_p = a/2$. The shear length can be seen to be a fraction of the original connection length $R_s \sim (r_p/a)q_a R$, where $q_a = (B_{p0}/B_t)(a/R)$ is the edge safety factor of a circular tokamak without the divertor coil. For the effective safety factor, $q_* \sim (r_p/a)q_a$. In the typical case of nearly equal currents $I_p = I_d$, the divertor is symmetric and $q_* \sim q_a \sim 2-5$. When $I_p > I_d$ the divertor becomes very compact in the sense that $r_p/a \sim 1/5 - 1/2$. In this case, one could obtain values as low as $q_* \sim 1$.

Although only indirectly related to the field line motion, let us also define two other useful coordinates: the Euclidean distance from the X-point $r = x^2 + y^2$ and the conformal conjugate coordinate that is orthogonal to ψ

$$\tau = (y^2 - x^2)/2. \tag{15}$$

IV. SOL CURRENT DENSITY

A. Spatial Structure

The current that is produced will flow along the field lines for a substantial distance from the divertor target. Dissipative effects (considered in Ref. [24]) lead to a decay of the parallel current on a length scale which is much longer than the characteristic distances of interest in this work, the shear length and divertor leg field line length. Because there is little perpendicular current, charge conservation implies that the parallel current density within a flux tube $J_\parallel/B$, must essentially be constant along a magnetic field line: $0 = \nabla\cdot\mathbf{J} \simeq$

$\mathbf{B}\cdot\nabla J_{\|}/B$. In the following, we neglect the variation of the field strength, and set $B =$ constant.

The parallel current density can only depend on the two constants of the field line motion ψ and ζ_0 defined in Eq. 13, and can be Fourier expanded over toroidal harmonics of ζ_0. Each toroidal harmonic n will be treated individually, so that one can assume

$$J_{\|}(\psi,\zeta_0) = J(\psi)\cos\left[n\zeta_0 + \chi(\psi)\right]. \tag{16}$$

The perturbation phase is defined by the argument of the cosine in Eq. 16,

$$\varphi = n\zeta + m_* \log\sqrt{y/x} + \chi(\psi). \tag{17}$$

The parameter

$$m_* = nq_* \sim nq_a(r_p/a) \tag{18}$$

regulates the phase coherence of the current density pattern in the vicinity of the X-point. If we estimate $q_a \sim 3$ and a large scale divertor with $r_p/a \sim 1$, then $m_* \sim 3n$. In a compact divertor where $r_p/a \sim 1/3$, then $m_* \sim n$.

Note that biasing the inner part of the strike point can also produce some current in the private flux zone. Because the current density is in phase along the divertor leg, the private flux current acts to enhance the perturbation field from the divertor leg. This current does not travel to the SOL, but over to the adjacent divertor leg. Since the region of large J_{sat} in the private flux zone is typically very thin, the contribution from the adjacent divertor leg will be neglected.

B. Phasing for Long vs. Short Divertor Legs

The phase structure of the current density in the plasma is sensitive to the phasing at the target plate. If the phase is constant radially across the target plate, there are two extreme cases where simple limits are realized: “long” divertor legs and “short” divertor legs, depending on the length of the divertor leg ℓ compared to the distance from the strike point to the biasing region δr and width Δr. We use this simple conceptually motivated terminology throughout, and the subscripts ℓ and 0 are used to distinguish the two cases, respectively.

For long divertor legs the divertor leg length ℓ is much larger than the location $\delta r = \delta\psi/\ell$ and width $\Delta r = \Delta\psi/\ell$ of the current profile at the target. Long divertor legs can be treated as the simple case where the perturbation is driven with constant phase radially along the location of the divertor target at $x = \ell$. In this case the phase is

$$\varphi_\ell(x) = n\zeta - m_* \log|\ell/x| + \chi_\ell \tag{19}$$

where χ_ℓ is the phase at the target at $x = \ell$ (on the plane $\zeta = 0$).

The parallel current density for long legs (Eq. 19) is shown in Fig. 4(a). One can see that along the divertor leg, there are large regions of current density which are all in phase. However, along the upper branch of the separatrix in the SOL, the pattern of current density becomes strongly sheared. The flux surfaces become aligned with the y direction, while the phase is still aligned with the x direction. Thus, above the X-point, the strong shear in field line motion causes the phase of the current density to vary across flux surfaces.

Often the divertor legs are short, a choice that can be used to enhance flux expansion at the target. In this case, the phase of the perturbation can be taken to be constant along a line that connects to the X-point. Figure 4(b) illustrates the current density pattern in the limit of extremely short divertor legs, where the phase is constant along the line $y = x$. In this case, the location is $\delta r = \sqrt{2\delta\psi}$, the width is $\Delta r \simeq \Delta\psi/\delta r$, and the phase would be

$$\varphi_0(y/x) = n\zeta - m_* \log\sqrt{|y/x|} + \chi_0 \tag{20}$$

where χ_0 is now the phase along the line $y = x$ near the X-point (on the plane $\zeta = 0$).

For the previous estimates in Sec. II D and II E, the long configuration was considered. However, for constant phase across the target, the angle of the target plate with respect to the magnetic field can also be used to interpolate between the two configurations. In a flexible biasing scenario with radial control over the phase, different configurations can be realized if the phase at the target plate can be used to compensate for the shearing of field lines along the leg. ITER may have some flexibility in this regard due to the sharply inclined target plates. The large target plate current density may also allow the biasing region to be placed further away to achieve the "short" configuration.

C. SOL Phase & Coherence Width

The phase difference between the current density on neighboring flux surfaces at ψ_a and ψ_b at a fixed point in y, can be determined by substituting the field line position along the divertor leg $x_{a,b} = \psi_{a,b}/y$ into Eqs. 19 and 20. For long legs, the result for the SOL phase difference

$$\Delta\varphi_\ell(y) = \varphi_{\ell,b} - \varphi_{\ell,a} = -m_* \log\left(\psi_b/\psi_a\right) \tag{21}$$

is completely independent of poloidal distance along the surfaces. Although the phase along a flux surface does vary poloidally, two neighboring flux surfaces always maintain the same phase difference far from the X-point. Because the phase depends logarithmically on ψ, a fact that was simply dictated by the field line motion, it is actually a ratio between radial positions that leads to a fixed phase difference. The current density between the flux surfaces will be out of phase once $\Delta\varphi = \pm\pi$. At this point, the ratio between the two radial positions can be taken to define the *coherence ratio*:

$$\kappa_\ell \equiv \psi_b/\psi_a|_{\Delta\varphi_\ell=-\pi} = \exp|\pi/m_*|. \tag{22}$$

The corresponding radial displacement can be taken to define the *coherence width*:

$$\sigma_\ell \equiv \psi_b - \psi_a|_{\Delta\varphi_\ell=-\pi} = 2\sqrt{\psi_a\psi_b}\,\sinh\left(|\pi/2m_*|\right), \tag{23}$$

which is defined relative to the geometric mean of the inner and outer positions. For $m_* >> \pi$, the coherence width becomes small since $\sigma_\ell/\psi \sim \pi/|m_*|$. For long legs, the special value $m_* = \pi\log 2 \simeq 4.5$ yields $\kappa_\ell = 2$ and $\sigma_\ell \simeq 71\%$ of the geometric mean. As an example, the shaded region in Fig. 2 represents a coherence region.

If the divertor legs are short, the phase coherence between neighboring flux surfaces is "doubled." The phase difference at constant y, is half of the previous result

$$\Delta\varphi_0(y) = -(m_*/2)\log\psi_b/\psi_a. \tag{24}$$

Thus, the coherence ratio in this case $\kappa_0 = \exp|2\pi/m_*|$ is κ_ℓ^2, the previous ratio squared (Eq. 22). Similarly, the coherence width $\sigma_0 = 2\sqrt{\psi_a\psi_b}\,\sinh\left(\pi/m_*\right)$ is twice as large as Eq. 23 at large m_*. Although the legs may be short, we note that the phase shearing is anti-symmetric across the line $x = y$, so that phase difference at constant x is simply $-\Delta\varphi_0$. For the special value $m_* = 4.5$, this yields $\kappa_0 = 4$ and the $\sigma_\ell = 150\%$ of the geometric mean.

Consider the phase differences between the three neighboring flux surfaces attached to the divertor target on the right-hand side of Fig. 5(a). The current density along these flux surfaces is shown in Fig. 5(b), where the independent axis is chosen to be a function of a coordinate which is always perpendicular to flux surfaces. The independent axis is actually chosen so that the phase is easily determined by visual inspection; the choice $\sinh^{-1}\tau$ causes the phase to vary periodically far from the X-point. The phases are meant to be compared to that along the reference surface (solid black). Along the divertor leg where $\tau \simeq -x^2/2 < 0$, one can see that all flux surfaces are in phase. However, in the SOL, where $\tau \simeq y^2/2 > 0$, the flux surface which is displaced inward by a factor of $\kappa_\ell^{-1/2} \simeq 0.71$ leads in phase by $\pi/2$, while the flux surface which is displaced outward by the factor $\kappa_\ell^{1/2} \simeq 1.4$ lags in phase by $\pi/2$. Hence, the two displaced flux surfaces are π out of phase with respect to one another.

V. EFFECTIVE SOL SURFACE CURRENT

A. Definition & Effect of Flux Expansion

Assume that the current density will be driven in a relatively thin layer surrounding the separatrix. On flux surfaces further away than the width of the current distribution, the perturbation will appear to be generated by what is effectively a parallel surface current density, $K_\parallel$. There are two distinct geometric effects that affect the result: flux expansion increases the surface current amplitude near the X-point, while the shearing of phase between neighboring flux surfaces causes a reduction of the net surface current as it travels beyond the X-point region.

The net surface current density $K_\parallel$ across flux surfaces is defined by the integral $K_\parallel = \int J_\parallel d\ell_r$, where ℓ_r is the radial distance orthogonal to the flux surfaces. This definition can be rewritten as

$$K_\parallel(\tau) = \int_{\psi_a}^{\psi_b} J_\parallel(\psi,\tau)d\psi/|\nabla\psi| \tag{25}$$

where the factor $|\nabla\psi| = r$, accounts for the flux expansion across the region. Far from the X-point, $K_\parallel = J_{avg}\Delta\psi/r$, where r is the distance to the region. Near the X-point, $K_\parallel = J_{avg}\Delta r \simeq J_{avg}\Delta\psi/\delta r$ for a thin region.

This simple definition leads to an important, yet counter-intuitive, dependence of $K_\parallel$ on flux expansion. If one were to integrate a purely poloidal current density $\mathbf{J}_p$ across a flux surface, one would obtain a poloidally-directed current. Current continuity $\nabla \cdot \mathbf{J} = 0$ ensures that this current is conserved and, thus, forces J_p to be inversely proportional to flux expansion. In this case, the purely parallel component $J_\parallel$ is conserved along a field line and must be independent of flux expansion. But then, integration across a flux tube implies that the surface current density must be proportional to flux expansion. This does not violate a conservation law, because one still needs to integrate over a poloidal distance to define a net current.

Physically, flux expansion causes the distribution of current density to expand in the direction normal to the flux surface and contract in the direction tangential to the flux surface as the X-point is approached. Conservation of the parallel current does occur over a region that contracts poloidally as it expands radially to conserve area; i.e. in flux coordinates. Consider displaying a very narrow current density profile in the conformal coordinates, $\Delta\psi = xy - \delta\psi$ and τ, which are designed to "unwrap" the current density along the mean flux surface. The resulting profile shown Fig. 6(a) clearly displays the way in which the extremal "lobes" of current density marked by the letters a,b,c,d,e must expand normally and contract tangentially as the X-point is approached. Since the surface current is parameterized by the direction along the surface, its magnitude must increase as its wavelength decreases in order to represent the same magnitude of total current in each peak. The result is shown in Fig. 6(b).

The discontinuity in the magnetic field perturbation must contain the same dependence on flux expansion. This increase is equal to the longer radial distance that one could bias a device with short divertor legs. For long divertor legs, flux expansion is determined by the distance to the target, while near the X-point, flux expansion is determined by the distance $r_X = \sqrt{2\delta\psi} = \sqrt{2\ell\delta r}$. Thus, the field perturbation near the X-point $\tilde{B}_X/\tilde{B}_{sat} = \ell/r_X = \sqrt{\ell/2\delta r}$ is even larger than that near the divertor leg. For ITER parameters, assuming $\ell \sim 1$ m, and $\delta r \sim 2 - 3$ cm, this leads to a factor of $\times 6 - 7$ enhancement.

The total current contained within one of the "lobes" in Fig. 4 is conserved and is equal to the total current passing through each of the $2n$ biasing regions. This current can be evaluated as the integral of the surface current density over a poloidal length that covers one half of a phase period:

$$I_{lobe} = \int_{\varphi=0}^{\varphi=\pi} d\ell_p K_\parallel. \tag{26a}$$

Since $d\ell_p = dy|B_p/B_y| = dy|r/y| = rd\varphi_\ell/m_*$, one obtains

$$I_{lobe} = \int_0^\pi d\varphi K_\| r/m_* = J_{avg}\Delta\psi/m_*. \tag{26b}$$

This is equal to the elementary result that would be obtained by integrating half of a period of the current passing through the divertor target $I_{lobe} = J_{avg}(B_p'\ell/B_t)R\Delta r/n = J_{avg}\ell\Delta r/m_*$. Estimates for the lobe current are given in Table I.

B. Current Drive Efficiency & Effect of Phase Interference

An even stronger effect is the phase interference that arises from the shearing of field lines near the X-point. Along the target plate, the phase is constant as one integrates across the flux surfaces, and all surfaces add coherently. However, above the X-point in the SOL, the destructive interference of the phases between neighboring flux surfaces causes the integrated surface current to depend on the width of the drive near the target in an oscillatory fashion. Since the surface current is simply an integral over the current density, the surface current will have an extremum whenever one of the edges satisfies $J_\|(\psi_{a,b}, y, \zeta) = 0$; i.e. at constant y.

For long divertor legs (Eq. 19), this leads to local maxima in the total surface current whenever the outer edge ψ_b satisfies

$$\log(\psi_b/\delta\psi) = (4p_b + 1)\pi/2m_* \tag{27}$$

for any integer p_b, where $\delta\psi$, is defined by the relation $m_* \log(k\delta\psi/y) = -(n\zeta + \chi)$. Local maxima also occur whenever the inner point ψ_a satisfies

$$\log(\psi_a/\delta\psi) = (4p_a - 1)\pi/2m_* \tag{28}$$

for any integer p_a. Thus, there are maxima when the ratio satisfies

$$\log(\psi_b/\psi_a) = (2p + 1)\pi/m_* \tag{29}$$

for some integer p. Optimization with respect to power consumption clearly requires all current density to be in phase, so that the width would stay below the coherence width $(p = 0)$.

Phase mixing is "half" as strong in the case of short divertor legs, where the drive is constant near the X-point. This is because the phase in Eq. 20 at constant y now depends on $(m_*/2)\log(\psi/y^2)$. This implies that for large m_* the surface current drive is twice as great as the case of long legs.

In the next two subsections, the goal will be to describe the efficiency with which current can be driven. Given the average distance of the current channel from the X-point $r_t = \ell, \sqrt{2\delta\psi}$ (long, short), one can define the efficiency in a manner that accounts for the natural variation due to flux expansion. Along the divertor leg

$$\varepsilon_{leg} = |rK_{leg}|/r_t K_{sat} \tag{30a}$$

for phase at constant x (evaluated at large x), and along the SOL

$$\varepsilon_{sol} = |rK_{sol}|/r_t K_{sat} \tag{30b}$$

for phase at constant y (evaluated at large y). The case of long legs is treated explicitly. The equations will still be valid for the SOL for the case of short legs after the replacement $m_* \to m_*/2$. The difference is that the case of short legs displays a symmetry across the line $x = y$, so that any divertor leg amplitude would be equivalent to the SOL amplitude.

C. Step-wise Constant Profile

Assume that the driven current density profile is approximately constant over the biasing region $\psi \in [\psi_a, \psi_b]$, as in the case of the shaded (thin blue) curve in Fig. 2. In the SOL, it is clear that only the last coherence width will positively reinforce the surface current. In Section II A, it was argued that for constant current density, the maximum surface current that can be drawn between $\psi_a = 0$ and ψ_b is $r_t K_{sat} = J_{avg}\psi_b$. The efficiency of current drive over the divertor leg is simply

$$\varepsilon_{leg} = |rK_{leg}|/r_t K_{sat} = \Delta\psi/\psi_b \tag{31}$$

(for large x at constant x).

Substitution of the phase (Eq. 19) into the expression for the surface current (Eq. 25) yields the result

$$rK_{sol} = \int_{\psi_a}^{\psi_b} J_{avg} \cos\left(n\zeta - m_* \log|\ell y/\psi| + \chi\right) d\psi \tag{32a}$$

$$= -\frac{J_{avg}\psi}{\sqrt{1+m_*^2}} \sin\varphi_{sol}\Big|_{\psi_a}^{\psi_b} \tag{32b}$$

$$\varphi_{sol} = \varphi_\ell - \arctan m_*^{-1}. \tag{32c}$$

(for large y at constant y). For a region that is thinner than the coherence width, the maxima of K_{sol} are close in value to K_{leg}. As the width approaches σ_ℓ, the SOL surface current will become smaller and develop a phase shift. For large m_*, the SOL current is reduced by a factor of $1/m_*$ and phase shifted by $\pi/2$. The surface current is maximized by using as large of an outer edge as possible and an inner edge exactly one coherence width away. For a width of σ_ℓ, the efficiencies are determined by the maximum over toroidal phase:

$$\varepsilon_{leg,cw} = 1 - \kappa_\ell^{-1} \tag{33a}$$

$$\varepsilon_{sol,cw} = (1 + \kappa_\ell^{-1})/\sqrt{1 + m_*^2}. \tag{33b}$$

Figure 7 (a) plots the efficiency ε_{sol} (thin blue) that is obtained for $m_* = 4.5$ as the inner edge is varied ψ_a when the outer edge is fixed at $\psi_b = 1$. One observes characteristic logarithmic oscillations on the scale of κ_ℓ, e.g. the maximum at $\psi_a = 0.5$. The oscillations become small as $\psi_a \to 0$. This is because as the inner edge is moved toward the strike point by a number of coherence ratios, the contribution from the inner edge becomes negligible once $\psi_b >> \psi_a$. Although the entire leg is utilized, the SOL efficiency drops to

$$\varepsilon_{sol,in} = 1/\sqrt{1 + m_*^2}. \tag{34}$$

The optimal value for a single coherence width is larger by $(1 + \kappa_\ell^{-1})$, but the improvement is always less than a factor of 2. For a wide region, the losses in other optimization criteria, such as limiting power consumption, may be more important to consider. Figure 7(b) shows the efficiency versus m_* for both cases. The horizontal axis has two scales representing both long and short divertor legs.

The definition of the surface current in Eq. 25 which connects the leg to the separatrix can be integrated directly for a step-wise constant profile current density of arbitrary thickness. Since we have already investigated the limiting values, rather than display the analytic expression, Fig. 8 displays the result of integrating Eq. 25 over different thicknesses of the current density layer for the case $m_* \simeq 4.5$ where the coherence ratio is 2. The independent axis is again chosen to be $\sinh^{-1} \tau$. If the outer position ψ_b is fixed, then for a thin bias region $\psi_a/\psi_b = 0.75$ shown by the dashed (blue) curve in the figure, the amplitude of the surface current is $rK_{sol} = 0.25$, in arbitrary units, both along the leg and in the SOL. As the inner point is brought in towards the exact coherence ratio $\kappa_\ell = 2$, the surface current amplitude at the target rises to 0.5 and it reaches the maximum SOL value $(1+0.5)/\sqrt{1+4.5^2} = 0.33$. As the inner point is brought all the way to the strike point, the target surface current rises to 2, while the SOL current is reduced to $1/\sqrt{1+4.5^2} = 0.22$, or 2/3 of the value for a single coherence width.

D. Exponentially Decaying Profile

Assume that the maximum current density profile decays to small values far enough away from the strike point due to the rapid decrease in plasma pressure and J_{sat}. The envelope of the driven current decays exponentially with e-folding length λ. Since the value of λ depends on flux expansion, it is most natural to define the e-folding length in flux space Λ^2. For instance, for long divertor legs, the e-folding length at the target is $\lambda_\ell = \Lambda^2/\ell$.

The radial profile of the current density is assumed to take the form

$$J(\psi) = J_{max} \exp\left(-\psi/\Lambda^2\right) \tag{35}$$

over the biasing region from ψ_a to ψ_b. The maximum surface current density that can be drawn from the target is $r_t K_{sat} = J_{max}\Lambda^2$. The leg current density simply satisfies

$$r|K_{leg}| = r_t K_{sat} \exp(-\psi/\Lambda^2)\Big|_{\psi_b}^{\psi_a} . \tag{36}$$

for phase at constant x (evaluated at large x). The SOL surface current is

$$rK_{sol} = r_t K_{sat} \mathrm{Re}(\Gamma(1+im_*, \psi/\Lambda^2) e^{i\varphi_{sol}})\Big|_{\psi_b}^{\psi_a} \tag{37a}$$

$$\varphi_{sol} = n\zeta - m \log\left(\ell y/\Lambda^2\right) + \chi_\ell \tag{37b}$$

for phase at constant y (evaluated at large y), where $\Gamma(1+im_*, \psi)$ is the appropriately defined incomplete gamma function.

Biasing the entire wetted area, as in the less flexible scenario, will only produce a relatively small SOL surface current when σ_ℓ is much smaller than Λ^2. The explanation is that neighboring coherence zones will nearly cancel, so that the "last" positively reinforcing coherence width will have much smaller current density than the peak. The asymptotic form of Eq. 37a for $\psi_a \to 0$ and $\psi_b \to \infty$ is

$$rK_{sol,all} \simeq r_t K_{sat} \sqrt{|2\pi m_*|} e^{-|m_*\pi/2|} \sin\varphi'_{sol} \tag{38a}$$

$$\varphi'_{sol} \simeq \varphi_{sol} - m_* + \mathrm{sign}(m_*)\pi/4. \tag{38b}$$

Thus, the efficiency is

$$\varepsilon_{sol,all} \simeq \sqrt{|2\pi m_*|}e^{-|m_*\pi/2|}. \tag{39}$$

In this limit, the result physically implies that the radial region that contributes most to the integrated value is near $\psi/\Lambda^2 \simeq |m_*\pi/2|$. The exponential factor yields a small value for the coherent SOL current for large m_*.

Strong phase mixing can be remedied by utilizing a biasing profile that has at least one sharp radial boundary. The key condition is that the edge potential must change over a radial scale that is much shorter than the coherence width. For instance, if the thickness of the biasing region is less than σ_ℓ, with sharp transitions to ground, then all radial points will add coherently. In this case, the amplitude of the integrated current density will peak at a location on the order of the decay length, instead of continuing to rise as in the case of constant profile. Hence, there will now be an optimal placement of both the mean position and the width. This phenomenon can be seen clearly from the asymptotic form of Eq. 37a for large m_*

$$rK_{sol,cw} \simeq \frac{r_t K_{sat}}{\sqrt{1+m_*^2}} \left(\frac{\psi}{\Lambda^2}\right) e^{-\psi/\Lambda^2} \sin\varphi_\ell \Bigg|_{\psi_a}^{\psi_b} \tag{40}$$

which peaks when $\psi = \Lambda^2$. The maximum amplitude over toroidal phase now occurs for exactly one coherence width with mean centered on the peak position $\sqrt{\psi_a\psi_b} = \Lambda^2$. This same choice optimizes the efficiency for the exact expression Eq. 39. The exact value is plotted versus the mean position in Fig. 7(a) (thick black). The large m_* estimate of the efficiencies is now

$$\varepsilon_{leg,cw} \simeq 2e^{-1}\sinh(\pi/2m_*) \tag{41a}$$

$$\varepsilon_{sol,cw} \simeq 2e^{-1}\cosh(\pi/2m_*)/\sqrt{1+m_*^2}. \tag{41b}$$

The essential difference between the exponentially decaying and the step-wise constant cases is that the current that can be drawn from the target is now reduced both by the smaller coherence width and by the smaller limiting amplitude at the optimal position.

If the biasing region is much wider than the radial decay length, then the maximum SOL current drive is obtained when one of the edges is placed near the peak at Λ^2. The optimal placement of the inner/outer edges can be found numerically by optimizing the efficiency

ε_{sol}. Both possibilities are shown as cases: wide inner region $\psi_a = 0$ (dotted red) and wide outer region $\psi_b \to \infty$ (dashed green) in Fig. 2. For large m_*, the efficiencies asymptotically approach

$$\varepsilon_{leg,in/out} \to e^{-1} \tag{42a}$$

$$\varepsilon_{sol,in/out} \to e^{-1}/\sqrt{1+m_*^2} \tag{42b}$$

but these formulae underestimate the efficiency at low m_*. Figure 7(a) plots the efficiency versus the edge placement for two cases. The case of the inner target is plotted vs. the inner edge position ψ_a (dotted red) for the fixed outer edge position $\psi_b \simeq 1.19$. This ψ_b yields the largest value of ε_{sol} as $\psi_a \to 0$. The case of the outer target is plotted vs. the outer edge position ψ_b (dashed green) for the fixed inner edge $\psi_a \simeq 0.924$. This ψ_a yields the largest value of ε_{sol} as $\psi_b \to \infty$. Again there are logarithmic oscillations with scale κ_ℓ, before the limiting values are reached. Figure 7(b) plots the efficiency numerically optimized over edge placement with the same color coding as the other figures. Note that at low m_*, the outer configuration can be as efficient as the optimal case of a single coherence width.

Phase mixing is weaker for short legs than for long legs. The preceding results are valid as long as one makes the replacement $m_* \to m_*/2$. Figure 7(b) shows the efficiency of ε_{sol} versus m_* for both long and short divertor legs by showing the relevant scales. If the entire target is biased, the analog of Eq. 38 leads to an 11% reduction for $m_* = 4.5$.

VI. SOL MAGNETIC PERTURBATION

The magnetic perturbation generated by the SOL current can be estimated from the tangential discontinuity of the field across the current carrying layer

$$\tilde{B}_{sol} = 2\pi K_{sol}. \tag{43}$$

In Part II, it will be shown that the SOL perturbation field is close to being completely pitch-resonant ($m = qn$) for flux surfaces near the SOL current. If one assumes that the SOL current is close enough to the separatrix and the q profile does not change too quickly, the detailed calculation for the resonant amplitude modifies the result by factors of order unity for flux surfaces within a region near the edge. Thus, the previous estimates for the SOL magnetic perturbation will also be an order of magnitude estimate for the RMP amplitude contributed by the SOL field

$$|\tilde{B}_{nm}^{sol}| \sim \varepsilon_{sol} \tilde{B}_{sat}. \tag{44}$$

Whether ELM control can be achieved depends on the threshold value of $\tilde{B}_{nm}/B_t$ and, thus, the SOL efficiency that must be achieved. For the parameters in Table II, estimates for $\tilde{B}_{sat}/B_t$ in Table II are larger than nominal values of $1-5\times10^{-4}$ by factors of $\sim 1-100$. This implies that one may require a wide range of efficiency. Table III lists the efficiencies that can be obtained for a variety of m_* for all of the radial biasing strategies that were discussed in Section V. This information is transposed in Table IV which shows the m_* required to achieve a given efficiency for the various techniques for the various target efficiencies. If only 10% efficiency is required, any optimization technique will suffice as long as $m_* \leq 4, 8$ (long, short). The short divertor leg configuration can exceed 25% efficiency even when biasing the entire target for $m_* = 3$, but achieving this efficiency with a long divertor leg would require at least one of the optimization techniques even for $m_* = 2$. Obtaining 50% efficiency requires a step-wise constant current density profile, unless the configuration can achieve $m_* \leq 1, 2$ (long, short).

In Part II, it will be shown that the divertor leg perturbation field produces an exponentially small RMP contribution at large m_*. The divertor leg perturbation field can make a contribution if the combination of m_* and divertor leg length cause the entire divertor leg current to be phase at a given toroidal angle. The characteristic value of the field produced in this case can be estimated by assuming that the entire lobe of current sits near the X-point and acts at approximately a distance a away:

$$\tilde{B}_{lobe} = 2I_{lobe}/ca. \tag{45}$$

This value is tabulated in Table II for comparison and could be useful for diagnostic purposes. The actual field that is generated depends on both the target efficiency and the way in which the near-target current sources are closed, which typically leads to faster than $1/r$ decay. The RMP produced is weaker than this estimate because much of this field is non-resonant.

VII. SUMMARY & DISCUSSION

A technique for analyzing the efficiency with which SOL currents will generate magnetic perturbations near the X-point of a diverted tokamak has been developed. The spatial pattern of the SOL current density that is generated when the divertor targets are biased in a toroidally asymmetric fashion was analyzed in detail. In particular, the amplitude of the coherent surface current density that would propagate from the divertor target into the SOL was determined quantitatively. It was shown that the phase coherence can be improved by using short rather than long divertor legs. The sensitivity to the radial profile of the driven current density was explored though profiles that are step-wise constant along the divertor target and those that exponentially decay. The amplitude of the RMPs that are generated by such currents was then qualitatively estimated. Part II (Ref. [36]) explores the spatial structure of the resulting field in detail, and derives asymptotic estimates of the Fourier spectrum of the field in magnetic coordinates. There, it shown that the qualitative estimates presented here have the correct order of magnitude.

The limiting ion saturation current densities for ITER are able to support an appreciable sheath current $J_{sat} \sim 100 - 440$ A/cm^2 that is large enough to drive a significant magnetic perturbation. After estimating the decay length of $2 - 3$ cm in which to drive the SOL current, the RMP upper limit is estimated from the surface current approximation $\tilde{B}_{sat} \sim 2\pi J_{sat}\Delta r/c \sim 100 - 800G$. The magnetic field perturbation near the X-point is even larger by a factor of $\sqrt{\ell/2\delta r} \sim 6 - 7$, due to considerations of flux expansion. This gain directly corresponds to the greater width over which one would be able to drive the current in a system with short divertor legs. If this surface current were to flow coherently through the SOL, the experimental ELM control criterion would be exceeded by factors of $20 - 200$.

A more quantitative analysis of phase interference in the SOL demonstrates that destructive phase mixing will occur unless the radial profile is thinner than the coherence width defined in Eq. 23. For a thin biasing region with long divertor legs, the perturbation field in the SOL will be equal to that along the leg, and one can estimate $|B_{sol}| = |B_{leg}|$. This scaling only persists as long as the radial width is below the coherence width σ_ℓ so that $m_* < \pi$. As the width is increased, the SOL current drive efficiency will be reduced by phase interference. For profiles that are as wide as the coherence width, the maximum surface current is smaller in the SOL than along the divertor leg by the factor $\sim 1/\sqrt{1+m_*^2}$ for long divertor legs and $\sim 1/\sqrt{1+(m_*/2)^2}$ for short legs. Optimization of the coherent surface current for RMP applications therefore requires low n or low q_* and leads to a compact divertor with "short" divertor legs. If the limiting profile decays exponentially, not all of the target can be utilized coherently and the limiting amplitude in the coherent region will be reduced. This case can be optimized if the biasing region has at least one sharp edge. Optimally choosing the inner or outer edge of a wide biasing region can still produce up to half of the maximum value attained for a single coherence width.

If enough plasma is present in the outer SOL to cause the width of the current profile to be considered an independent parameter, this could increase the range of performance of the ELM control technique. In previous experiments on DIII-D [52], the biasing current density achieved in the outer SOL was observed to be larger than that determined by the original particle fluxes. In Ref. [52] (Figs. 3 and 4), heating of the plasma by the biasing technique was implicated in changing the characteristics of the plasma above the sheath and even in adding plasma to the far SOL.

Finally, note that the passive biasing techniques outlined in Ref. [23] are much better designed for a high-power tokamak environment. Actively generating negative bias potentials ϕ_b will accelerate the ions to higher incident energies and induce the additional ion heat flux $\Delta Q_i = -e\phi_b n_e u_i$. Likewise, positive bias potentials will reduce the ion heat flux. If the total flux $Q = \gamma T_e n_e u_i$ is defined by the sheath transmission factor, estimated to be $\gamma \sim 7 - 8$, then the relative change in heat flux can be as large as $\Delta Q/Q \sim e\phi_b/\gamma T_e \sim 1/4 - 1/2$. Although this additional heat flux is only a fraction of the original, one must assume that the issue of large steady-state divertor heat fluxes can be solved with some margin. The electric potential perturbation associated with the SOL current will act to cause additional convection of turbulent heat flux and may help to mitigate this effect [23, 24]. Taken together, the combination of non-axisymmetric SOL current and electrostatic convection may be a powerful technique for solving the problem of high target heat fluxes.

Acknowledgments

The authors would like to thank T. D. Rognlien for providing access to UEDGE divertor physics modeling results for ITER and for valuable discussions that lead to great improvements in this manuscript. We would also like to thank the referee for urging us to treat the effects of phase interference. This work was performed under the auspices of the U.S. Department of Energy by Lawrence Livermore National Laboratory under Contract

DE-AC52-07NA27344.

---

[1] M. Kotschenreuther, P. M. Valanju, S. M. Mahajan and J. C. Wiley, Phys. Plasmas **14**, 072502 (2007).

[2] F. Najmabadi and the ARIES Team, Fusion Eng. Des. **38**, 3 (1997).

[3] G. Federici, A. Loarte and G. Strohmeyer, Plasma Phys. Control. Fusion **45**, 1523 (2003).

[4] D. J. Campbell, Phys. Plasmas **8**, 2041 (2001).

[5] ITER Physics Expert Group on Divertor, ITER Physics Expert Group on Divertor Modelling and Database and ITER Physics Basis Editors, *The ITER Physics Basis*, Nucl. Fusion **39**, 2391 (1999).

[6] A. Loarte, B. Lipschultz, A. S. Kukushkin, G. F. Matthews, P. C. Stangeby, N. Asakura, G. F. Counsell, G. Federici, A. Kallenbach, K. Krieger, A. Mahdavi, V. Philipps, D. Reiter, J. Roth, J. Strachan, D. Whyte, R. Doerner, T. Eich, W. Fundamenski, A. Herrmann, M. Fenstermacher, P. Ghendrih, M. Groth, A. Kirschner, S. Konoshima, B. LaBombard, P. Lang, A.W. Leonard, P. Monier-Garbet, R. Neu, H. Pacher, B. Pegourie, R. A. Pitts, S. Takamura, J. Terry, E. Tsitrone, the ITPA Scrape-off Layer and Divertor Physics Topical Group, *Progress in the ITER Physics Basis*, Nucl. Fusion **47**, S203 (2007).

[7] A. S. Kukushkin, H. D. Pacher, G. Federici, G. Janeschitz, A. Loarte, G. W. Pacher, Fusion Eng. Des. **65**, 355 (2003).

[8] H. R. Wilson and R. L. Miller, Phys. Plasmas **6**, 873 (1999).

[9] P. B. Snyder, H. R. Wilson, J. R. Ferron, L. L. Lao, A. W. Leonard, T. H. Osborne, A. D. Turnbull, D. Mossessian, M. Murakami, and X. Q. Xu, Phys. Plasmas **9**, 2037 (2002).

[10] J. L. Luxon, Nucl. Fusion **42**, 614 (2002).

[11] P. H. Rebut, R. J. Bickerton and B. E. Keen, Nucl. Fusion **25**, 1011 (1985).

[12] T. E. Evans, R. A. Moyer, K. H. Burrell, M. E. Fenstermacher, I. Joseph, A. W. Leonard, T. H. Osborne, G. D. Porter, M. J. Schaffer, P. B. Snyder, P. R. Thomas, J. G. Watkins and W. P. West, Nature Phys. **2**, 419 (2006).

[13] K. H. Burrell, T. E. Evans, E. J. Doyle, M. E. Fenstermacher, R. J. Groebner, A. W. Leonard, R. A. Moyer, T. H. Osborne, M. J.

Schaffer, P. B. Snyder, P. R. Thomas, W. P. West, J. A. Boedo, A. M. Garofalo, P. Gohil, G. L. Jackson, R. J. La Haye, C. J. Lasnier, H. Reimerdes, T. L. Rhodes, J. T. Scoville, W. M. Solomon, D. M. Thomas, G. Wang, J. G. Watkins and L. Zeng,
Plasma Phys. Control. Fusion **47**, B37 (2005).

[14] Y. Liang, H. R. Koslowski, P. R. Thomas,
E. Nardon, B. Alper, P. Andrew, Y. Andrew, G. Arnoux, Y. Baranov, M. Becoulet, M. Beurskens, T. Biewer, M. Bigi, K. Crombe, E. De La Luna, P. de Vries, W. Fundamenski, S. Gerasimov, C. Giroud, M. P. Gryaznevich, N. Hawkes, S. Hotchin, D. Howell, S. Jachmich, V. Kiptily, L. Moreira, V. Parail, S. D. Pinches, E. Rachlew, and O. Zimmermann,
Phys. Rev. Lett. **98**, 265004 (2007).

[15] I. Joseph, R. A. Moyer, T. E. Evans, M. J. Schaffer, A. M. Runov, R. Schneider, S. V. Kasilov, M. Groth, M.E. Fenstermacher, J. Nucl. Mater. **363-365**, 591 (2007).

[16] I. Joseph, T. E. Evans, A. M. Runov,
M. E. Fenstermacher, M. Groth, S. V. Kasilov, C. J. Lasnier, R. A. Moyer, G. D. Porter, M. J. Schaffer, R. Schneider and J. G. Watkins,
Nucl. Fusion **48**, 045009 (2008).

[17] M. F. Heyn, I. B. Ivanov, S. V. Kasilov, W. Kernbichler, I. Joseph, R. A. Moyer, and A. M. Runov, Nucl. Fusion **48**, 024005 (2008).

[18] M. Bécoulet, E. Nardon, G. Huysmans, W. Zwingmann, P. Thomas, M. Lipa, R. Moyer, T. Evans, V. Chuyanov, Y. Gribov, A. Polevoi, G. Vayakis, G. Federici, G. Saibene, A. Portone, A. Loarte, C. Doebert, C. Gimblett, J. Hastie and V. Parail, Nucl. Fusion **48**, 024003 (2008).

[19] M. J. Schaffer, J. E. Menard, M. P. Aldan, J. M. Bialek, T. E. Evans and R. A. Moyer, Nucl. Fusion **48**, 024004 (2008).

[20] ITER Technical Basis, *Plant Description: Tokamak Systems Design & Assessment*, (International Atomic Energy Agency, Vienna, 2001).

[21] ITER Physics Expert Group on Disruptions, Plasma Control and MHD, and ITER Physics Basis Editors, Nucl. Fusion **39**, 2251 (1999).

[22] S. J. Zinkle, Phys. Plasmas **12**, 058101 (2005).

[23] R. H. Cohen and D. D. Ryutov, Nucl. Fusion **37**, 621 (1997).

[24] D. D. Ryutov, P. Helander and R. H. Cohen, Plasma Phys. Control. Fusion **43**, 1399 (2001).

[25] R. H. Cohen, D. D. Ryutov, G. Counsell and P. Helander, Plasma Phys. Control. Fusion **49**,

1 (2007).

[26] A. Sykes, R. J. Akers, L. C. Appel,
E. R. Arends, P. G. Carolan, N. J. Conway, G. F. Counsell, G. Cunningham, A. Dnestrovskij, Yu. N. Dnestrovskij, A. R. Field, S. J. Fielding, M. P. Gryaznevich, S. Korsholm, E. Laird, R. Martin, M. P. S. Nightingale, C. M. Roach, M. R. Tournianski, M. J. Walsh, C. D. Warrick, H. R. Wilson, S. You, MAST Team and NBI Team,
Nucl. Fusion, **41** 1423 (2001).

[27] G. F. Counsell, R. H. Cohen, P. Helander, D. D. Ryutov and the MAST Team, 30th EPS Conference on Contr. Fusion and Plasma Phys., St. Petersburgh, 2003, edited by R. Koch and S. Lebedev (European Physical Society, 2003), Europhysics Conference Abstracts **27A** P-3.202, http://epsppd.epfl.ch/StPetersburg/PDF/P3_202.PDF

[28] G.F. Counsell, J.-W. Ahn, R. Akers, E. Arends, S. J. Fielding, P. Helander, A. Kirk, H. Meyer, A. Tabasso, H. Wilson, Y. Yang, J. Nucl. Mater. **313-316** 804 (2003).

[29] G.F. Counsell, J.-W. Ahn, R.H. Cohen, A. Kirk, P. Helander, R. Martin, D.D. Ryutov, A. Tabasso, H.R. Wilson, Y. Yang and the MAST team, Nucl. Fusion **43** 1197 (2003).

[30] G. M. Staebler and F. L. Hinton, Nucl. Fusion **29**, 1820 (1989).

[31] G. M. Staebler, Nucl. Fusion **36**, 1437 (1996).

[32] R. Fitzpatrick, Phys. Plasmas **5**, 3325 (1998).

[33] A. Cole and R. Fitzpatrick, Phys. Plasmas **13**, 032503 (2006).

[34] J.-K. Park, M. J. Schaffer, J. E. Menard, and A. H. Boozer, Phys. Rev. Lett. **99** 195003 (2007).

[35] J.-K. Park, A. H. Boozer, J. Menard, Nucl. Fusion **48** 045006 (2008).

[36] I. Joseph, *Driving toroidally asymmetric current through the tokamak scrape-off layer, Part II: Magnetic field structure and spectrum*, submitted to Phys. Plasmas (2009).

[37] P. C. Stangeby, *The Plasma Boundary of Magnetic Fusion Devices*, (Institute of Physics Pub., London, 2000).

[38] J. G. Watkins, P. Stangeby, J. A. Boedo, T. N. Carlstrom, C. J. Lansier, R. A. Moyer, D. L. Rudakov, D. G. Whyte, J. Nucl. Mater. **290-293** 778 (2001).

[39] J. G. Watkins, D. Taussig, R. L. Boivin, M. A. Mahdavi, and R. E. Nygren, Rev. Sci. Instr. **79** 10F125, (2008).

[40] J.G. Watkins, T.E. Evans, M. Jakubowski, R.A. Moyer, O. Schmitz, A. Wingen,

M.E. Fenstermacher, I. Joseph, C.J. Lasnier, D.L. Rudakov, J. Nucl. Mater. (2009), doi:10.1016/j.jnucmat.2009.01.221.

[41] M. E. Fenstermacher, S. L. Allen, N. H. Brooks, D. A. Buchenauer, T. N. Carlstrom, J. W. Cuthbertson, E. J. Doyle, T. E. Evans, P.-M. Garbet, R. W. Harvey, D. N. Hill, A. W. Hyatt, R. C. Isler, G. Jackson, R. A. James, R. Jong, C. C. Klepper, C. J. Lasnier, A. W. Leonard, M. A. Mahdavi, R. Maingi, W. H. Meyer, R. A. Moyer, D. G. Nilson, T. W. Petrie, G. D. Porter, T. L. Rhodes, M. J. Schaffer, R. D. Stambaugh, D. M. Thomas, S. Tugarinov, M. R. Wade, J. G. Watkins, W. P. West, D. G. Whyte, and R. D. Wood, Phys. Plasmas **4**, 1761 (1997).

[42] W. Fundamenski, S. Sipil and JET-EFDA contributors, Nucl. Fusion **44**, 20 (2004).

[43] A. Kallenbach, N. Asakura, A. Kirk, A. Korotkov, M.A. Mahdavi, D. Mossessian, G.D. Porter, J. Nucl. Mater. **337-339**, 381 (2005).

[44] A. S. Kukushkin, H. D. Pacher, G. W. Pacher, G. Janeschitz, D. Coster, A. Loarte and D. Reiter, Nucl. Fusion **43**, 716 (2003).

[45] R. Schneider, X. Bonnin, K. Borrass, D. P. Coster, H. Kastelewicz, D. Reiter, V. A. Rozhansky, and B. J. Braams, Contrib. Plasma Phys. **46**, 3 (2006).

[46] T. D. Rognlien, J. L. Milovich, M. E. Rensink and T. B. Kaiser, J. Nucl. Mater. **196-198**, 347 (1992).

[47] T. D. Rognlien, *private communication*,
(2008).

[48] D. Farina, R. Pozoli and D. D. Ryutov, Nucl. Fusion **33**, 1315 (1993).

[49] D. D. Ryutov and R. H. Cohen, Contrib. Plasma Phys. **48**, 48 (2008).

[50] S.S. Abdullaev, K.H. Finken, M. Jakubowski and M. Lehnen, Nucl. Fusion **46**, S113 (2006).

[51] S. S. Abdullaev, M. Jakubowski, M. Lehnen, O. Schmitz, and B. Unterberg, Phys. Plasmas **15**, 042508 (2008).

[52] G. M. Staebler, Nucl. Fusion **220-222**, 158 (1995).

TABLE I: Estimates for the range of parallel ion saturation current density that can be driven for typical parameters of three different tokamaks.

	R	a	ℓ	λ	n_e	T_e	J_{max}	K_{sat}	$m_* I_{lobe}$
	cm	cm	cm	cm	10^{13}cm^{-3}	eV	Acm^{-2}	Acm^{-1}	kA
ITER	620	200	100	2-3	20-200	1-20	100-400	200-1000	20-100
DIII-D	165	55	20	2-3	1-20	1-40	5-40	10-100	0.2-3
MAST	85	65	100	2-5	0.05-0.3	10-40	0.4-2	0.7-9	0.07-1

TABLE II: Upper limits for the magnetic field perturbation corresponding to the parameters of Table I. The resonant field in the SOL must be multiplied by the efficiencies ε_{sol}.

	B_t	$\tilde{B}_{sat}$	$\tilde{B}_{sat}/B_t$	$m_* \tilde{B}_{lobe}$	$m_* \tilde{B}_{lobe}/B_t$
	10^4G	G	10^{-4}	G	10^{-4}
ITER	5.3	100-800	20-200	20-100	4-30
DIII-D	2.0	6-80	3-40	0.7-10	0.4-5
MAST	0.5	0.4-6	0.9-10	0.04-0.6	0.1-1

TABLE III: The SOL efficiency in % (Eq. 30b) obtained for various optimized geometric configurations. Labels: “step”=step profile, “exp”=exponential profile, “cw” = single coherence width, “out”=optimized outer target plate, “in”=optimized inner target plate, ”all” = entire target plate.

$m_* =$	1	2	3	4	long
$m_* =$	2	4	6	8	short
step cw	74	54	43	35	
step in	71	45	32	24	
exp cw	60	35	24	18	
exp out	60	31	17	11	
exp in	53	23	14	10	
exp all	52	15	4	1	

TABLE IV: The value of m_* required to obtain various levels of SOL efficiency (Eq. 30b) for various geometric configurations. Smaller values of m_* would achieve higher ε_{sol}. Included for reference are the short leg values which are exactly 2× the long leg values. Labels; see Table III.

	long			short		
$\varepsilon_{sol} =$	50%	25%	10%	50%	25%	10%
step cw	2.3	6.4	18.4	4.6	12.7	36.8
step in	1.7	3.9	9.9	3.5	7.7	19.9
exp cw	1.3	2.9	7.3	2.6	5.7	14.7
exp out	1.3	2.3	4.2	2.5	4.6	8.4
exp in	1.1	1.9	3.9	2.1	3.8	7.9
exp all	1.0	1.6	2.3	2.1	3.2	4.6

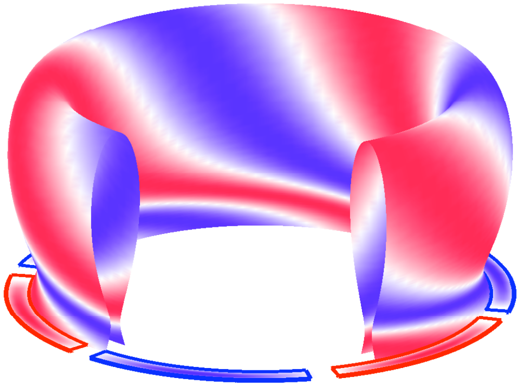

FIG. 1: (Color online) Profile of the $n = 3$ parallel current perturbation that would be driven by alternately biasing the target at a set of 6 locations on the divertor floor near the outer strike point.

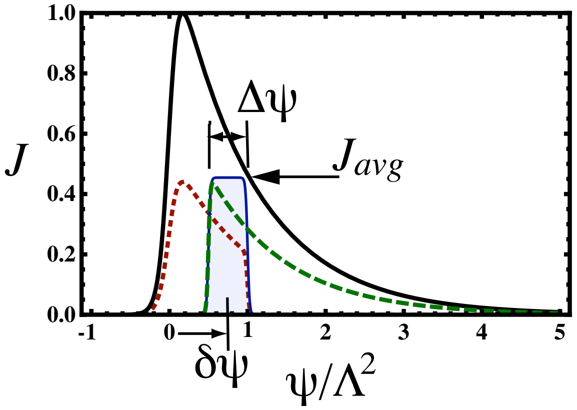

FIG. 2: (Color Online) The driven current density profile across the target with mean value J_{avg}, distance from the strike point $\delta\psi$, and width $\Delta\psi$ is limited by the ion saturation current $J_{sat} \sim \exp(-\psi/\Lambda^2)$ (thick black). Possible radial profiles depending on the biasing geometry: thin region equal to one coherence width for $m_* = 4.5$, $\psi/\Lambda^2 = [0.5, 1]$ (thin blue); wide inner region $\psi/\Lambda^2 = [0, 1]$ (dotted red); wide outer region $\psi/\Lambda^2 = [0.5, \infty]$ (dashed green).

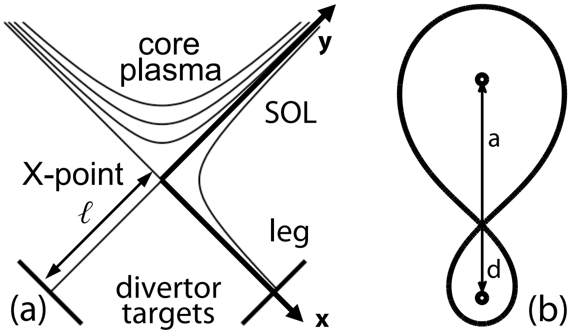
core
plasma
y
SOL
X-point
ℓ
leg
(a)
divertor
targets
x
a
d
(b)

FIG. 3: (a) The divertor region near the X-point. (b) The separatrix defining the magnetically confined plasma, private flux, and scrape off layer regions for a simple two-wire model.

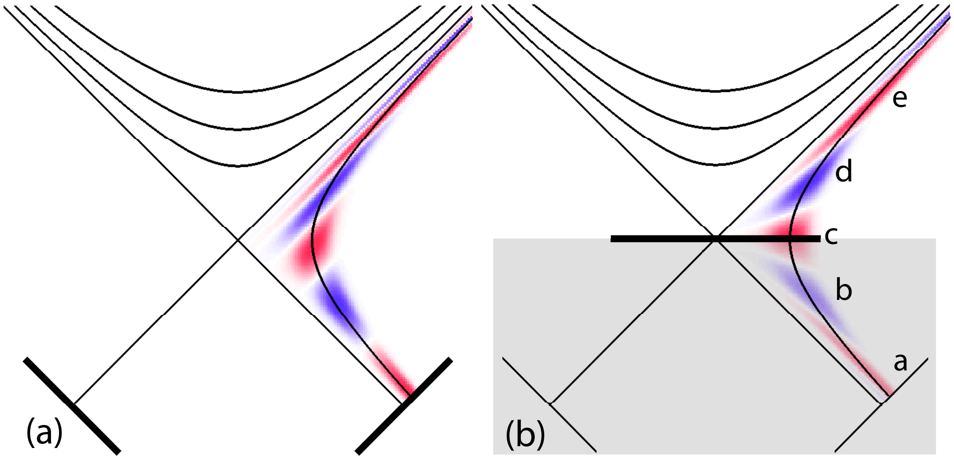

FIG. 4: (Color online) Contours of the parallel current density, assumed to be constant along field lines, for the case $m_* = 4.5$ and $\ell/\delta = 25$. The current source takes constant phase within the toroidal plane $\zeta = 0$ and across the target plate for (a) long legs $x = \ell$ (Eq. 19) and (b) short legs $y = x$ (Eq. 20). Black hyperbolic lines denote flux surfaces and letters a,b,c,d,e mark distinct extrema of current density.

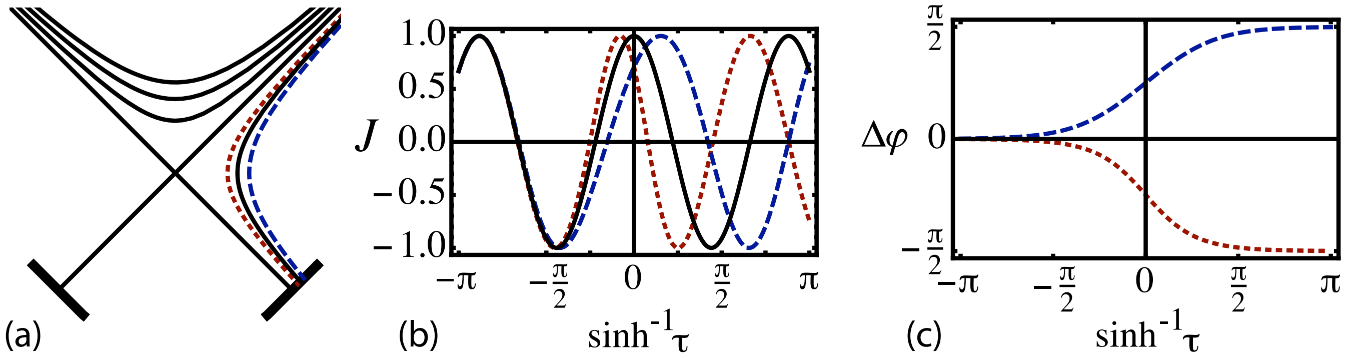

FIG. 5: (Color online) For the three radially separated flux surfaces connected to the target shown in (a), the current density (b) and phase difference (c) is shown as a function of $\sinh^{-1}\tau$ (Eq. 15) for constant ζ. Here, $m_* = 4.5$ which corresponds to Fig. 4(a). The solid black curve is located at an arbitrary reference position $\delta\psi$ that defines $\Delta\varphi = 0$. Inner surface: $\psi \simeq 0.71\delta\psi$ (dotted red); outer surface: $\psi \simeq 1.4\delta\psi$ (dashed blue).

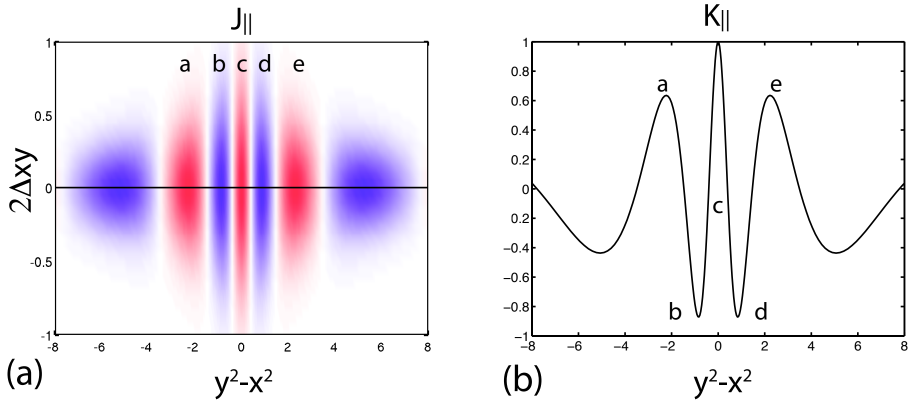

FIG. 6: (a) (Color online) Color contours of a thin parallel current density profile after "unwrapping" along the central flux surface. (b) The magnitude of the surface current density (normalized to the peak value) needed to represent the current density in part (a). Letters a,b,c,d,e mark the same extrema as in Fig. 4(b).

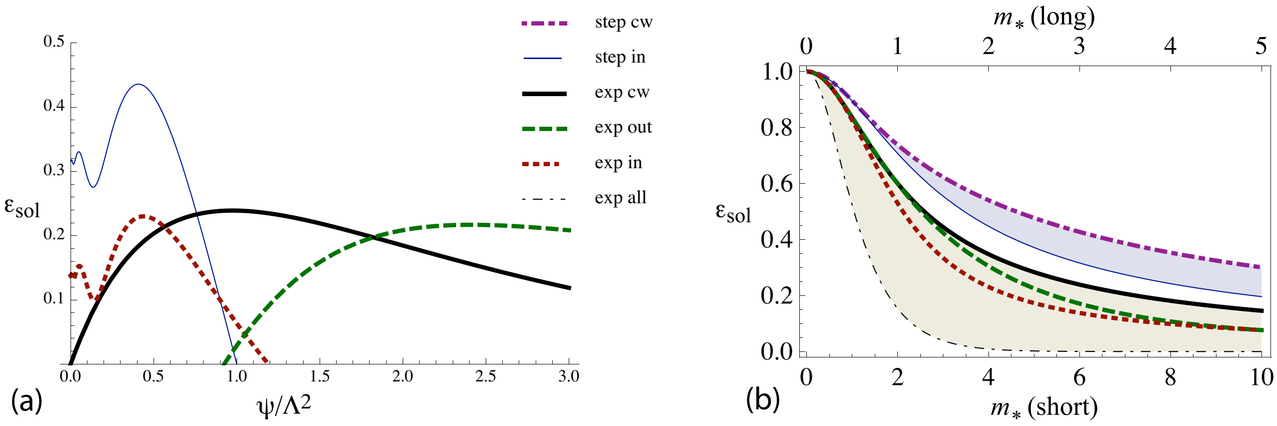

FIG. 7: (Color online) (a) The SOL surface current drive efficiency ε_{sol} (Eq. 30b) for various geometric configurations of the biasing region; $m_* = 4.5, 9$ for long, short legs. Step profile plotted vs. inner edge ψ_a with outer edge $\psi_b = 1$ (thin blue). Exponential profiles: plotted vs. inner edge ψ_a with optimum outer edge $\psi_b \simeq 1.19$ (dotted red); plotted vs. outer edge ψ_b with optimum inner edge $\psi \simeq 0.924$ (dashed green); plotted vs. mean $\sqrt{\psi_a \psi_b}$, single coherence width (thick black). (b) Efficiency vs. m_*: bottom axis for short legs, top axis for long legs. Labels: "Step" profiles $\psi_b = 1$ (shaded blue): "cw" = single coherence width (dot-dashed purple); "in" = inner target plate $\psi_a = 0$ (thin blue). "Exp"onential profiles (shaded grey): "cw" = single coherence width, optimum $\sqrt{\psi_a \psi_b} = 1$ (thick black); "in" = inner target plate $\psi_a = 0$ with optimized outer edge ψ_b (dotted red); "out" = outer target plate $\psi_b \to \infty$ with optimized inner edge ψ_a (dashed green); "all" = entire target (thin dot-dashed black).

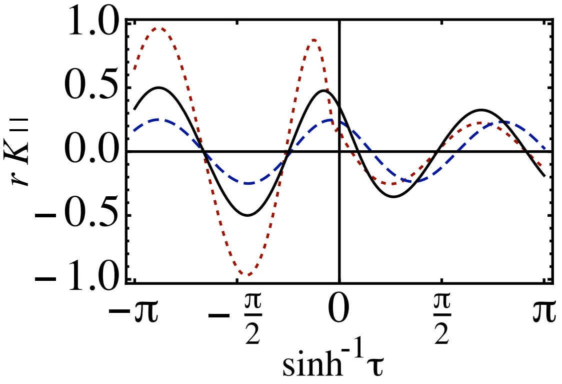

FIG. 8: (Color online) The surface current density defined by Eq. 25 is shown versus $\sinh^{-1}\tau$ (Eq. 15) for various thicknesses of current density; same case as Fig. 4(a): short divertor legs and $m_* = 4.5$. The outer edge ψ_b is fixed, while the inner edge ψ_a is varied: a "thin" region $\psi_a/\psi_b = 0.75$ has the same maxima along both the leg and the SOL (dashed blue); the largest SOL surface current is achieved at the coherence ratio $\psi_a/\psi_b \simeq 0.5$ (solid black); the inner edge is moved to the strike point $\psi_a = 0$ (dotted red).